scientific reports

Check for updates

OPEN

A Raman probe of phonons and electron–phonon interactions in the Weyl semimetal $NbIrTe_4$

Iraj Abbasian Shojaei[1], Seyyedesadaf Pournia[1], Congcong Le[2,3], Brenden R. Ortiz[4,5], Giriraj Jnawali[1], Fu-Chun Zhang[2], Stephen D. Wilson[4,5], Howard E. Jackson[1] & Leigh M. Smith[1]✉

There is tremendous interest in measuring the strong electron–phonon interactions seen in topological Weyl semimetals. The semimetal $NbIrTe_4$ has been proposed to be a Type-II Weyl semimetal with 8 pairs of opposite Chirality Weyl nodes which are very close to the Fermi energy. We show using polarized angular-resolved micro-Raman scattering at two excitation energies that we can extract the phonon mode dependence of the Raman tensor elements from the shape of the scattering efficiency versus angle. This van der Waals semimetal with broken inversion symmetry and 24 atoms per unit cell has 69 possible phonon modes of which we measure 19 modes with frequencies and symmetries consistent with Density Functional Theory calculations. We show that these tensor elements vary substantially in a small energy range which reflects a strong variation of the electron–phonon coupling for these modes.

Three dimensional topological semimetals have attracted intense interest in recent years[1–5]. These materials are enabled by broken spatial or time inversion symmetries, and the large spin orbit interactions which collapses the conduction and valence bands within a limited section of the Brillouin zone where the conduction and valence bands cross and invert. Dirac, Weyl, nodal-line, and nested fermion semimetals have all been predicted theoretically and observed experimentally[6–11]. Weyl semimetals are particularly interesting since pairs of Weyl nodes with opposite chirality appear as monopole sources and sinks of Berry curvature[12,13]. This results in unusual transport properties such as the anomalous Hall effect, extremely large and non-saturating magneto-resistance, the chiral anomaly and negative longitudinal magneto-resistance[14–19]. In addition, extremely large nonlinear optical effects such as sum and difference frequency generation, nonlinear DC shift currents (electromagnetic rectification), and photoinduced anomalous Hall effect have been predicted and observed[20–25]. The Weyl semimetals are classified in two flavors: Type-I, which approximately maintain Lorentz invariance, and Type-II where the linear crossings are tilted as to result in electron and hole pockets in the Fermi surface at the Weyl point[26–28].

Recently, both theoretical and experimental evidence demonstrate that the electron–phonon interactions in Weyl semimetals can provide insights into the electronic structure of these unusual materials. For example, calculations show that one can use magnetic field effects on phonons in Weyl semimetals in both enantiomorphic[29] and mirror-symmetric[30] materials as a direct result of the chiral anomaly. Phonon-mediated changes in hydrodynamic flow in WTe2 have also very recently been measured[31]. Changes in the phonon dispersion, optical reflectivity and Raman scattering are expected[29,30,32,33]. Evidence for the strong coupling between phonons and Weyl Fermions is seen by Fano resonances observed in temperature tuned TaAs (IR reflectivity)[34], temperature-dependent Raman measurements in NbAs, TaAs and WP2[35,36], and also in Resonant Raman Scattering in TaP[37]. The chiral anomaly in NbAs was seen in phonon measurements using magnetic field-dependent IR reflectivity measurements[38]. In this paper we use polarized angular-resolved Raman scattering in $NbIrTe_4$, a possible Type II Weyl semimetal, to show that one can extract the Raman tensor elements for each phonon mode from the *shape* of the scattering efficiency versus angle. Thus the electron–phonon coupling for individual phonon modes can be measured for different excitation energies.

Weyl semimetals are only possible for materials which break either spatial inversion symmetry or time inversion symmetry, or both[3]. The two-dimensional $NbIrTe_4$ material is a ternary alloy which is analogous to

[1]Department of Physics, University of Cincinnati, Cincinnati, OH, USA. [2]Kavli Institute of Theoretical Sciences, University of Chinese Academy of Sciences, Beijing 100190, China. [3]Max Planck Institute for Chemical Physics of Solids, 01187 Dresden, Germany. [4]Materials Department, University of California Santa Barbara, Santa Barbara, CA 93106, USA. [5]California Nanosystems Institute, University of California Santa Barbara, Santa Barbara, CA 93106, USA. ✉email: leigh.smith@uc.edu

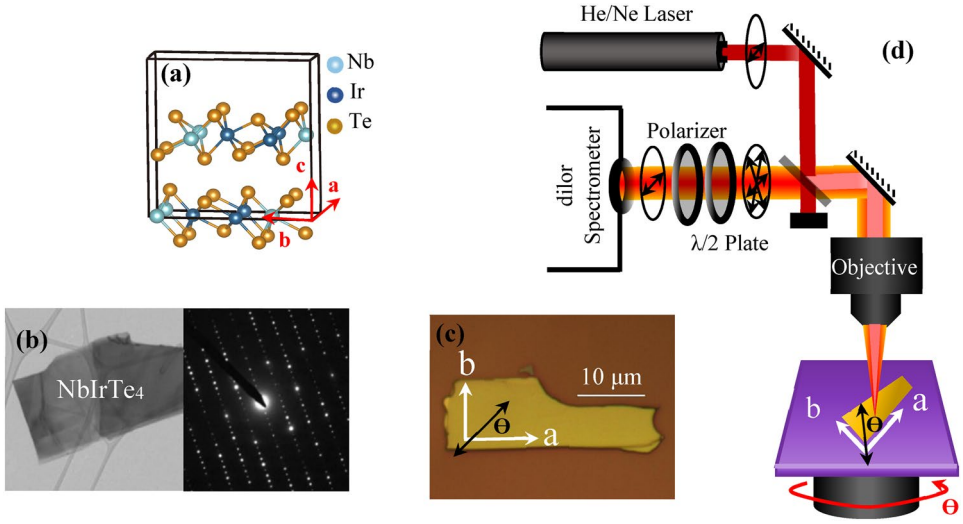

Figure 1. (**a**) Schematic side perspective of crystal structure of $NbIrTe_4$. (**b**) TEM image and TEM diffraction pattern of $NbIrTe_4$ along c-axis. (**c**) The optical image of the $NbIrTe_4$ sample including 'a' and 'b' crystal line axes and the polarization direction of the incident light. (**d**) The schematic diagram of polarized Raman measurement with rotational stage.

the known Type-II Weyl semimetal WTe_2, so it is expected to break inversion symmetry. Several ab initio calculations including spin–orbit coupling indicate that $NbIrTe_4$ is a type-II Weyl semimetal with 16 Weyl points which contains 8 pairs of opposite chirality located at energies very close to the Fermi energy[39]. With 24 atoms per unit cell, 69 phonon modes are possible in this structure[40]. While several magneto-transport measurements in late 2019 have shown non saturating magneto-resistance at low temperature, and quantum oscillations[41,42] which are consistent with a complex Fermi surface, there are no angle-resolved photoemission spectroscopy (ARPES) measurements to investigate the expected surface Fermi arcs or band crossings expected in this material.

In the first section, we describe angle-resolved polarized micro-Raman scattering measurements on a nanoflake of $NbIrTe_4$ to investigate the symmetry and frequency of the Stokes scattered Raman modes. We show that the observed modes and symmetries are consistent with *ab-initio* density functional theoretical (DFT) calculations and extract the normal modes of atomic vibrations for these modes.

Then we consider whether there is evidence of variable electron phonon interactions for different laser excitations. We compare in detail the symmetries and intensities of the observed Raman active modes in $NbIrTe_4$, which are excited at 633 nm (red) and at 514 nm (green) wavelengths. We observe enhanced intensity for most Raman modes for 633 nm excitation, and also a notable variation between the two excitation wavelengths for different rotational symmetries of the modes which identify changes in the electron–phonon interaction. These changes with excitation wavelength vary substantially from mode to mode. We conclude with a discussion which shows that we can extract detailed information about each of the Raman tensor elements (electron–phonon coupling constants) for 13 phonon modes ranging from 45 to 260 cm^{-1} (5–32 meV).

Sample morphology and experimental setup

A single crystal ternary $NbIrTe_4$ alloy was grown by the flux method (see Methods). The orthorhombic primitive cell of this structure (Fig. 1a) includes 24 atoms with four formula units[43]. Chains of Nb and Ir atoms alternatively follow a zigzag pattern along the 'a' axis, and hybridize with each other long the 'b' axis to form a conducting plane. Te atoms bond on top and bottom of the 'ab' planes to form layers which are van der Waals bonded along the 'c' direction[43].

A transmission electron microscopy (TEM) image and electron diffraction pattern of $NbIrTe_4$ sample taken along the 'c' direction is illustrated at Fig. 1b. The TEM diffraction pattern is taken with the electron beam aligned with the central part of a $NbIrTe_4$ exfoliated flake dispersed onto a holey carbon grid. The TEM image exhibits the uniformity of the exfoliated flake, while the diffraction pattern confirms the symmetry of the orthorhombic structure of this material with the a and b directions of the diffraction pattern corresponding to the 'a' and 'b' axes of the flake.

X-ray diffraction measurements (XRD) from a $NbIrTe_4$ single crystal grown in the same way determined lattice constants of 3.79(03), 12.52(07) and 13.14(35) Angstroms for the 'a', 'b' and 'c' lattice constants, respectively. These lattice constants are very close to the calculated values in the literature[43] and are used as inputs to our DFT calculation (see Methods) in order to obtain appropriate interatomic potentials for this crystal. Details of the DFT calculations are in the supplementary document (S1).

The nanoflakes were exfoliated from a $NbIrTe_4$ single crystal by using NITTO blue tape, and then mechanically transferred on a Si/SiO_2 substrate for angle-resolved polarized micro-Raman spectroscopy (see optical image in Fig. 1c).

Figure 1d illustrates a schematic diagram of our polarized micro-Raman experiment system (see Methods). A linearly polarized 632.9 nm or 514.5 nm laser is focused to a ~ 1.5 μm spot onto the nanoflake with the optic axis aligned parallel to the 'c' axis of the nanoflake. The substrate with the nanoflake is rotated keeping the laser spot fixed so that the polarization is at an angle θ relative to the 'a' axis (Fig. 1c). The double-sided black arrow in the image shows the polarization direction of the incident light relative to the 'a' and 'b' axes of the nanoflake marked by white arrows. A polarization analyzer is set so that the polarization of the scattered light (e_s) is either parallel ($e_i \parallel e_s$) or perpendicular ($e_i \perp e_s$) to the incident laser polarization (e_i). Data for both configurations is collected with a 10 minute exposure time with the sample rotated through 360 degrees with 10-degree increments.

Experimental and theoretical results

The orthorhombic primitive cell of $NbIrTe_4$ structure belongs to the space group $Pmn2_1$ or point group C_{2v} including 4 irreducible representations, $A_{1,2}$ and $B_{1,2}$. From the character table, the $NbIrTe_4$ unit cell includes 24 atoms so that 72 phonon modes are possible with 69 Raman-active modes: $23\,A_1 + 12\,A_2 + 11\,B_1 + 23\,B_2$. Detecting modes with different irreducible representations can be achieved by selecting the laser excitation direction along with the polarization configuration of the experiment.

The incoming and backscattered beams are along the 'c' axis of $NbIrTe_4$ lattice (see Fig. 1d), and perpendicular to the nanoflake. We align the 'x', 'y' and 'z' directions of lab coordinate system with the 'a', 'b' and 'c' crystallographic axes of the structure, respectively. The angle θ is thus between the polarization direction of the incident beam and the 'x' axis. The Raman experiments are taken either in the parallel configuration ($e_i \parallel e_s$) or in the perpendicular configuration ($e_i \perp e_s$).

We recall that the scattered intensity in Raman experiments is proportional to the excitation frequency and polarization direction of the incident and scattered light[44]:

$$I(\theta, \varphi, \omega_s) = A\omega_s^4 |\mathbf{e_i}.\mathbf{R}.\mathbf{e_s}|^2 \tag{1}$$

$$R \sim \sum_{\alpha,\beta} \frac{\langle f|H_{eo}|\beta\rangle\langle\beta|H_{ep}|\alpha\rangle\langle\alpha|H_{eo}|i\rangle}{(E_L - (E_\beta - E_i) - \hbar\omega_v - i\gamma)(E_L - (E_\alpha - E_i) - i\gamma)}$$

where A provides the scaling with incident laser power, ω_i and ω_s are the frequencies of the incident and scattered photons, **R** is the Raman tensor reflecting selection rules and containing the electron–phonon coupling parameters, $\mathbf{e_i}$ and $\mathbf{e_s}$ are the incident and scattered polarization vectors. E_L is the incident laser energy, E_α and E_β are the energies of the intermediate electronic states $|\alpha>$ and $|\beta>$, ω_v is the phonon frequency, E_i is the energy of the initial electronic state. H_{eo} and H_{ep} are the electron-photon and electron–phonon operators. Thus the denominator describes resonance conditions for the incoming and outgoing photons[44]. After removing the ω_s^4 dependence, the normalized scattered intensities at two different excitation wavelengths provide a view into the Raman tensor dependence on crystal orientation and excitation energy and geometry for each mode and thus connect that to the electron–phonon interactions in this material. The Raman tensors corresponding to the A_1, A_2, B_1 and B_2 irreducible representations are given by[45,46]

$$R_{A_1} = \begin{pmatrix} d & 0 & 0 \\ 0 & f & 0 \\ 0 & 0 & g \end{pmatrix} R_{A_2} = \begin{pmatrix} 0 & h & 0 \\ h & 0 & 0 \\ 0 & 0 & 0 \end{pmatrix} R_{B_1} = \begin{pmatrix} 0 & 0 & 0 \\ 0 & 0 & k \\ 0 & k & 0 \end{pmatrix} R_{B_2} = \begin{pmatrix} 0 & 0 & l \\ 0 & 0 & 0 \\ l & 0 & 0 \end{pmatrix} \tag{2}$$

where d, f, g, h, k and l are complex tensor elements of **R** which depend on the derivatives of the complex dielectric response and are connected to the electron–phonon coupling between electronic and lattice states[47]. Each complex element includes a phase term in the form of the $x = |x|e^{i\varphi_x}$.

According to Porto's notation, we see from Eq. (2) that the $Z(XX)\overline{Z}$ and $Z(YY)\overline{Z}$ measurements (θ = 0° and θ = 90° when $e_i \parallel e_s$) reveal A_1 modes and, $Z(XY)\overline{Z}$ and $Z(YX)\overline{Z}$ measurements (θ = 0° and θ = 90° when $e_i \perp e_s$) reveal A_2 modes. Also, because the incident and scattered light propagates along 'c' (z) axis direction (the electric fields are parallel to the xy plane for any θ), Raman experiments do not probe the B_1 or B_2 phonon modes.

For the incident laser polarization at an angle of θ relative to the a axis, the elements of $\mathbf{e_i}$ and $\mathbf{e_s}$ are (cos(θ), sin(θ), 0) for the $e_i \parallel e_s$ a measurement, while for the $e_i \perp e_s$ measurement $\mathbf{e_s}$ has (− sin(θ), cos(θ), 0) elements. Thus, at a fixed excitation frequency, by using $\mathbf{e_i}$ and $\mathbf{e_s}$ in Eq. (1), the intensity of Raman modes as a function of rotation angle will take the form:

$$I_{A_1} = |d|^2\cos^4(\theta) + |f|^2\sin^4(\theta) + 2|d||f|\cos^2(\theta)\sin^2(\theta)\cos(\varphi_{df}) \tag{3}$$

$$I_{A_1} = \cos^2(\theta)\sin^2(\theta)\left[|d|^2 + |f|^2 - 2|d||f|\cos(\varphi_{df})\right] \tag{4}$$

$$I_{A_2} = |h|^2\sin^2(2\theta) \tag{5}$$

$$I_{A_2} = |h|^2\cos^2(2\theta) \tag{6}$$

$$I_{B_1} = I_{B_1} = I_{B_2} = I_{B_2} = 0 \tag{7}$$

where $\varphi_{df} = \varphi_d - \varphi_f$ is the relative complex phase factor between the d and f tensor elements. From this result we see that the angular dependence of the A_1 intensity when measured in the parallel configuration depends

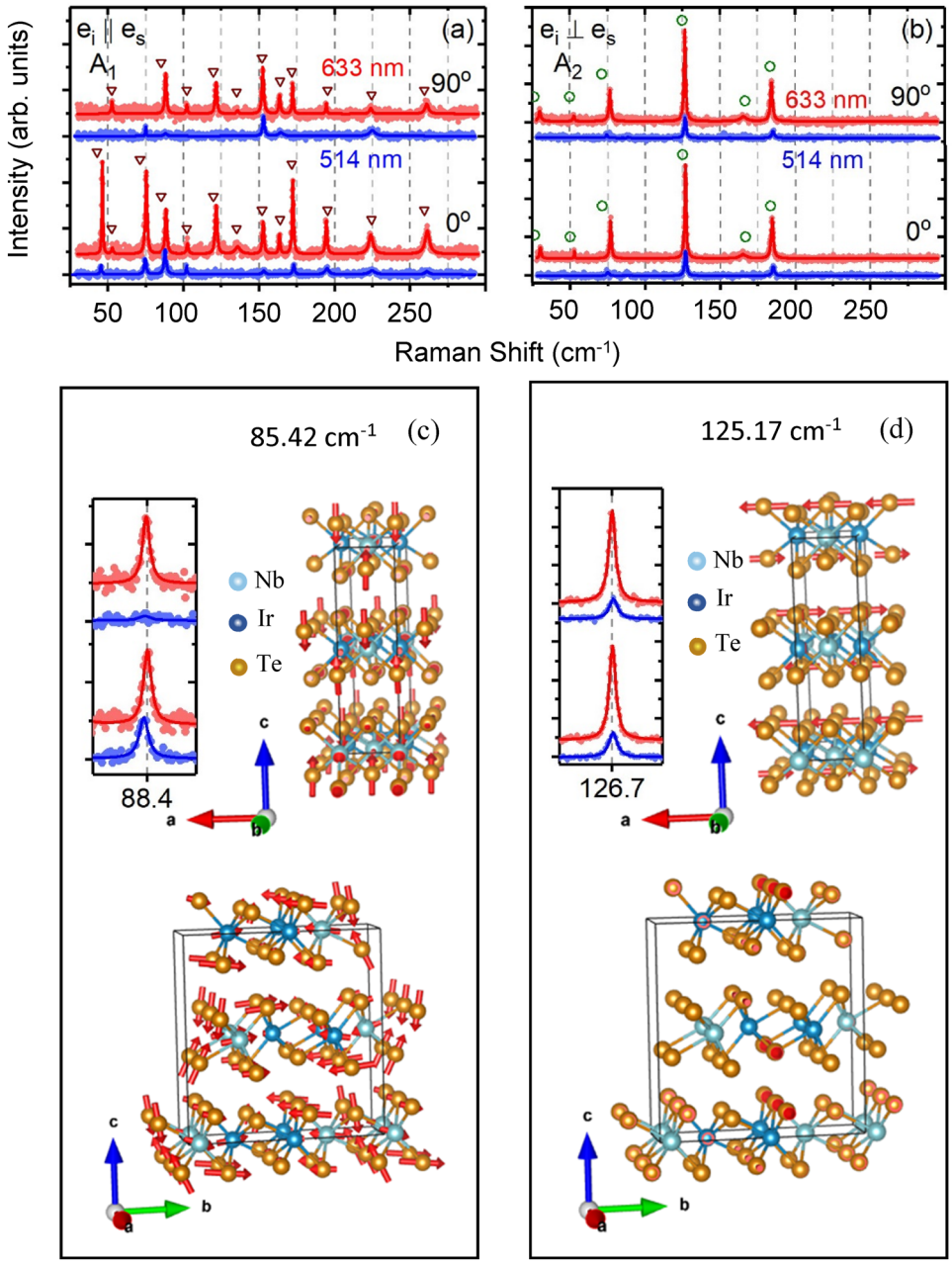

Figure 2. Polarized Raman spectra of $NbIrTe_4$ nano-flake as a function of rotation angle. (**a**, **b**) Raman spectra for two selected angles (0°, 90°) between polarization direction of the incident beam and a-axis of the sample, respectively, for parallel and cross configurations. Red and blue lines are Lorentz fittings of the Raman spectra measured with 633 nm and 514 nm laser excitation, respectively. Dark red triangles and green circles illustrate the calculated Raman frequencies of the detected modes by Density Functional Theory belonging to the A_1 and A_2 irreducible representations, respectively. (**c**, **d**) Simulated normal modes of given frequencies calculated by the Density Function Theory at two perspectives for a one selected A_1 mode at 85.42 cm^{-1} and one selected A_2 mode at 125.17 cm^{-1}, respectively. The direction of arrows shows the direction of the atoms vibration and magnitude of arrows represent relative amplitude of atoms vibration.

strongly on the d and f elements, which reflect the electron–phonon coupling. For all other measurements, the angular dependence only depends on geometry. The |d|/|f| ratio and φ_{df}, thus have an important role in the angular behavior of the A_1 Raman modes which is discussed in supplementary documents (S2, S3)[47].

As noted previously, [Eqs. (3)–(6)], one can distinguish that for $Z(XX)\overline{Z}$ and $Z(YY)\overline{Z}$ measurements only A_1 modes can be seen while for $Z(XY)\overline{Z}$ and $Z(YX)\overline{Z}$ measurements only the A_2 modes are observed. Figure 2a, b show Raman spectra for $(Z(XX)\overline{Z}, Z(YY)\overline{Z})$ and $(Z(XY)\overline{Z}, Z(YX)\overline{Z})$ respectively, with a Lorentz fit to all spectral lines observed for 633 nm (red curve) and 514 nm (blue curve) excitations. 13 A_1 and 6 A_2 Raman modes are

Mode Type in $Pmn2_1$	DFT Calculation (cm^{-1})	$e_i \parallel e_s$ 633 nm (cm^{-1})	$e_i \parallel e_s$ 514 nm (cm^{-1})	$e_i \perp e_s$ 633 nm (cm^{-1})	$e_i \perp e_s$ 514 nm (cm^{-1})	$e_i \parallel e_s$ I_{633}/I_{514}	|d|/|f| 633 nm	|d|/|f| 514 nm	φ_{df}(°) 633 nm	φ_{df}(°) 514 nm
A_1	42.84	46.4	45.6	46.2	45.9	8.3	2.5	1.2	94	64
A_1	52.52	–	–	56.3	–	–	1	–	90	–
A_1	71.35	75.4	75.2	75.4	75.6	4.6	3.1	1.5	105	96
A_1	81.45	–	–	–	–	–	–	–	–	–
A_1	85.42	88.4	88.0	88.4	88.0	1.7	1	2.1	90	84
A_1	102.16	102.3	102.1	102.3	–	1.3	1	1.8	90	12
A_1	107.51	–	–	–	–	–	–	–	–	–
A_1	119.86	121.7	–	121.7	–	∞	1.2	–	47	–
A_1	134.01	–	–	–	–	–	–	–	–	–
A_1	135.31	135.9	–	135.9	–	∞	1.4	–	130	–
A_1	139.86	–	–	–	–	–	–	–	–	–
A_1	152.11	152.5	153.2	152.5	153.3	2.5	0.8	0.6	120	112
A_1	162.47	–	–	–	–	–	–	–	–	–
A_1	163.97	164.0	164.0	–	–	3	1	0.8	20	47
A_1	171.64	172.4	173.4	172.4	–	7.1	1.5	2.3	50	72
A_1	187.48	–	–	–	–	–	–	–	–	–
A_1	192.10	–	–	–	–	–	–	–	–	–
A_1	195.31	194.4	195.0	194.4	–	3.7	1.6	1.9	54	44
A_1	220.88	–	–	–	–	–	–	–	–	–
A_1	224.53	224.1	225.2	224.1	–	2.5	1.4	1	51	32
A_1	259.45	261.2	260.7	261.2	–	6.5	1.2	1.2	94	10
A_1	266.05	–	–	–	–	–	–	–	–	–
A_2	26.55	–	–	30.3	–	–				
A_2	50.23	–	–	52.6	–	–				
A_2	56.60	–	–	–	–	–				
A_2	71.59	77.0	–	77.0	–	–				
A_2	99.57	–	–	–	–	–				
A_2	103.68	–	–	–	–	–				
A_2	124.54	–	–	–	–	–				
A_2	125.17	126.7	126.8	126.7	126.8	2.5				
A_2	159.87	–	–	–	–	–				
A_2	166.94	–	–	165.0	–	–				
A_2	182.00	–	–	–	–	–				
A_2	183.83	184.5	185.3	184.35	185.3	2.8				

Table 1. Calculated A_1 and A_2 Raman modes of the $NbIrTe_4$ nano-flake by using density functional theory (DFT) and experimentally extracted values in parallel and cross configurations using 633 nm and 514 nm excitation. The last four columns express the parameters d/f and ϕ_{df} determined from the angular dependence for each experimentally detected A_1 modes.

observed. These measurements have been calibrated utilizing a helium gas discharge near 514 and 633 nm which provide a spectral resolution and linewidth of around 1 cm^{-1} (see S4). The linewidths of the detected Raman modes are around 1 cm^{-1} (limited by our instrument resolution) except 2 modes at 224.1 and 261.2 cm^{-1} which show a 3.5 cm^{-1} linewidth. This confirms the high crystal purity of our samples. Comparison to DFT calculations for both A_1 and A_2 modes is exhibited by dark red triangles and green circles, respectively. Except for 3 A_1 modes (42.84 cm^{-1}, 52.52 cm^{-1}, 71.35 cm^{-1}) and 2 A_2 modes (26.55 cm^{-1}, 71.59 cm^{-1}) which are within 7% of the DFT frequencies, the remaining 14 detected mode frequencies agree within 2% or less of the DFT frequencies. The exact values of our measurements for A_1 and A_2 Raman frequencies and DFT calculations are listed in Table 1. In this table all 35 $A_{1,2}$ modes predicted by DFT calculations are listed. The predicted values of the $B_{1,2}$ modes can be found in the in the supplementary documents (S5). The details of the DFT calculations which provide both the frequency and symmetry of active Raman modes are provided in the supplementary documents (S1).

Figure 2c, d show spectra and fits to a representative A_1 and A_2 mode at both red (633 nm) and green (514 nm) excitations. The frequencies extracted from these fits are 88.4 cm^{-1} for the A_1 mode and 126.7 cm^{-1} for the A_2 mode. For comparison, the frequency of the DFT calculated mode is shown as symbols: 85.42 cm^{-1} for the A_1 mode (3% error) and 125.17 cm^{-1} for the A_2 mode (1% error). The atomic vibrations for these two modes are shown with two different perspectives, namely viewed along either the 'a' or 'b' axis. Note that the motion of atoms for the A_1 modes is restricted to the 'cb' crystal plane, while the atoms for the A_2 modes can only vibrate parallel

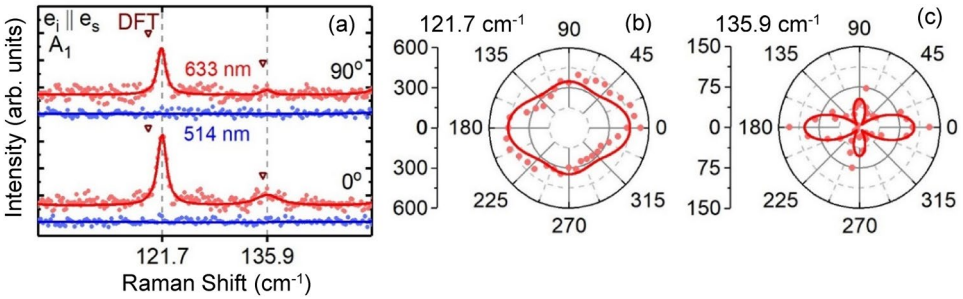

Figure 3. (**a**) Raman spectra for two peaks at angles of 0°, 90° for the parallel polarization configuration with 633 nm excitation (red lines) and 514 nm (blue lines) excitation. Dark red triangles mark the calculated modes utilizing Density Function Theory. (**b**, **c**) Polar plots of the Raman modes at 121.7 cm^{-1} and 135.9 cm^{-1} respectively using 633 nm excitation.

to the 'a' axis of the crystal. This is true for all modes with these symmetries. For the A_1 mode at 85.42 cm^{-1} all Nb, Ir and Te atoms are seen to move, while for the A_2 mode at 125.17 cm^{-1} only some of the tellurium atoms move. The details about the atomic vibrations for other modes are in the supplementary documents (S6).

Comparing the Raman spectra in Fig. 2 obtained for green (514 nm) or red (633 nm) laser excitation, one can immediately see that generally the scattering efficiencies for most modes increase strongly for red excitation. From Eq. (1) the scattering efficiency usually is dominated by the ω^4 term which thus would increase the intensities for green excitation. In order to see clearly the change in the matrix elements, the spectra in this paper are normalized to the measured integrated intensity of the well-known 520 cm^{-1} silicon (optical phonon) Raman line. This removes both the ω^4 term and any dependence of the measurement from the Raman instrument and detector. By comparison with reflectivity measurements in the closely related materials $TaIrTe_4$[48] and WTe_2[49] we do not expect any large change in the dielectric response (real or imaginary parts) with laser excitation energy which might also impact the Raman measurements. The penetration depth is also substantially less than the nanoflake thickness. The normalized intensity ratios (I_{633}/I_{514}) for each mode are recorded in Table 1. While two modes at 85.42 cm^{-1} and 102.16 cm^{-1} do not show significant change, the two modes at 119.86 cm^{-1} and 135.31 cm^{-1} are not detected for 514 nm excitation at all. There are no modes which show a weaker response for red laser excitation, and most show an enhancement of the matrix element by a factor of 2–8. As we shall now discuss, there are also strong changes in the angular dependence of A_1 modes measured for $e_i \parallel e_s$ for different excitation energies.

The Raman tensor, Raman intensities and variation of electron phonon interaction

As captured by Eqs. 1–7, the intensity of the Raman scattering for different modes depends on both the values of |d|, |f|, and |h| as well as the geometry as reflected in the angle θ. We will see that presentation of the data in polar plots reflects this variation and note that, as well, the response can be significantly different for the two different excitation wavelengths.

Figure 3a illustrates a segment of our $Z(XX)\overline{Z}$ and $Z(YY)\overline{Z}$ Raman measurements where two 121.7 and 135.9 cm^{-1} modes are only observed with 633 nm excitation (red dots and line); no response of these modes is observed for 514 nm excitation measurements (blue dots and line). Thus, these two modes clearly demonstrate a strong dependency on excitation energy suggesting that the coupling between electronic states and lattice states is very weak for 514 nm excitation. Fitting spectra of our angle-resolved measurements with the $e_i \parallel e_s$ configuration for these two modes is obtained by fixing the frequency and varying only the linewidth and intensity for all fits. The results of the intensity versus angle are fit to Eq. (3), as shown with solid lines in Fig. 3b, c. As detailed in the supplementary information (S2), these plots allow us to extract the relative value of '|d|' and '|f|' for each mode. For instance, for the mode at 121.7 cm^{-1}, |d| and |f| are nearly equal. For the mode at 135.9 cm^{-1} |d| is about 40% larger than |f|.

The other observed 10 A_1 modes can be classified into two categories. In one category, regardless the effect of φ_{df} on rotational symmetry of the modes (S3), the |d|/|f| ratio stays either larger than or smaller than one as the excitation energy is changed. Figure 4 shows polar plots of 6 modes at two 633 nm (red curves) and 514 nm (blue curves) excitations for a $e_i \parallel e_s$ configuration. This figure displays 5 modes at 46.4, 75.4, 172.4, 194.4 and 261.2 cm^{-1} where the maximum for both excitation wavelengths is along 'x' direction with the ratio of |d|/|f| larger than 1 (S2) for both excitations. We see that the maximum of plot at 152.5 cm^{-1} is along 'y' direction which means |d|/|f| is smaller than 1 for both excitations.

For each of these 10 modes, we note that the integrated intensity with 633 nm excitation is *larger* than for the comparable 514 nm measurements. The blue numbers within each plot show the factor by which the of 514 nm measurements are multiplied to have equal intensity with 633 nm measurements. As noted in Table 1, this factor is different for each mode, with the largest value of 8.3 for the mode at 46.4 cm^{-1} and the smallest value of 1.3 for 102.2 cm^{-1}.

In the second category, which includes 4 (different) modes, the |d|/|f| ratio equals one for one excitation and is distinctly different from one for another excitation. Figure 5 shows polar plots of 4 modes at both excitation

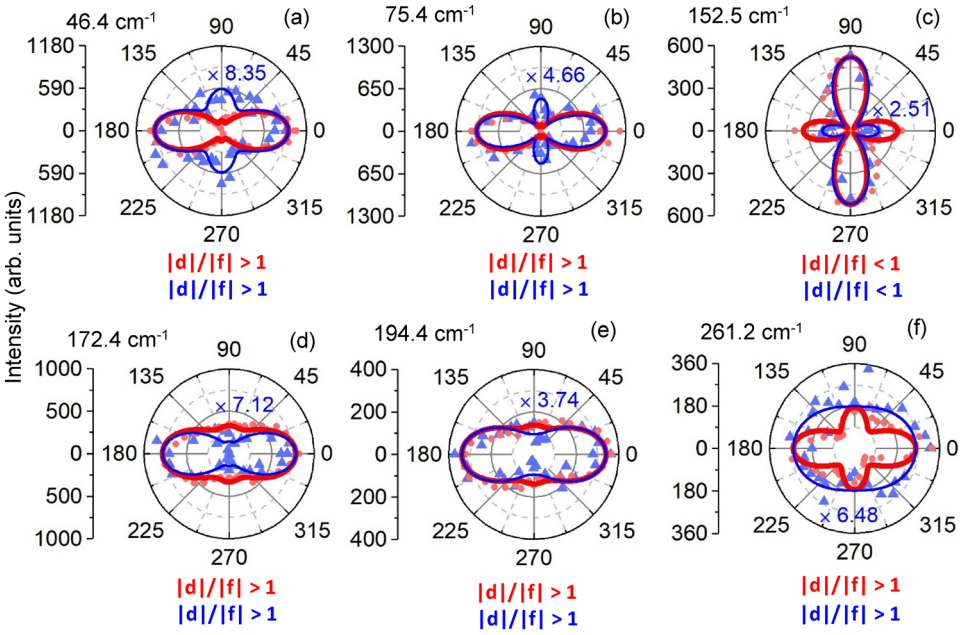

Figure 4. Intensity polar plots (**a**–**f**) of six observed Raman modes of $NbIrTe_4$ with a |d|/|f| ratio of larger or smaller than 1 for both excitation wavelengths. In (**c**) the ratio of |d|/|f| is smaller than 1 and all others are larger than 1. Red (blue) curves illustrate theoretical fitting of measurements for 633 nm (514 nm) excitation. To facilitate comparison, a magnification is applied for each Raman mode measured at 514 nm excitation (blue number within plot).

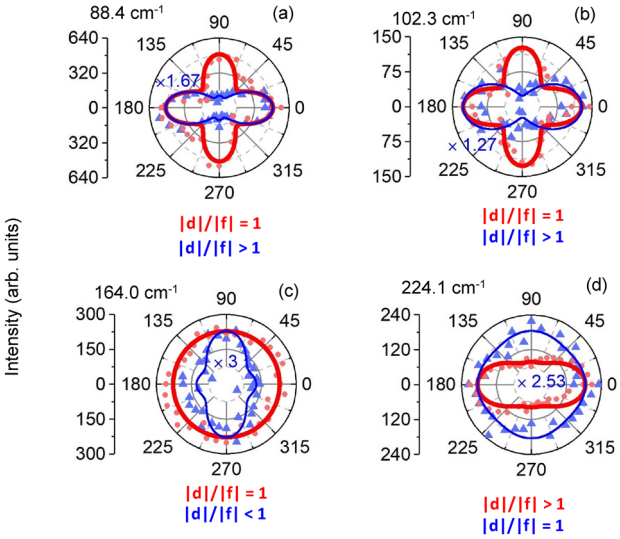

Figure 5. Intensity polar plot of four observed Raman modes of $NbIrTe_4$ with |d|/|f| ratio equals 1 for one of the excitation energies. Plots (**a**–**c**) show modes where just for measurement of the 633 nm excitation the ration of |d|/|f| equals 1, and plot (**d**) shows the mode where just for measurement of the 514 nm excitation the ration of |d|/|f| equals 1. Red (blue) curves illustrate theoretical fitting of measurement by 633 nm (514 nm) laser beam. The factor of magnification for each Raman mode measured by 514 nm laser is declared by blue number at each plot.

wavelengths for the $e_i \parallel e_s$ configuration. One can see that the |d|/|f| ratio equals 1 for the 633 nm measurements for modes at 88.4, 102.3, and 164 cm^{-1} modes; in contrast, for 514 nm excitation |d|/|f| is larger than 1 at 88.4 (|d|/|f|= 2.1) and 102.3 cm^{-1} (|d|/|f|= 1.8) and is smaller than 1 at 164 cm^{-1} (|d|/|f|= 0.8) for 514 nm excitation. For mode at 224.1, |d|/|f| ratio equals 1 for the 514 nm measurements while for 633 excitation |d|/|f| equals 1.5. Clearly coupling between electron and lattice states strongly depends on excitation energy for these modes.

Symmetry	f (cm^{-1})	I_{633}/I_{514}	$\lvert d_{633}\rvert/\lvert d_{514}\rvert$	$\lvert f_{633}\rvert/\lvert f_{514}\rvert$
A1	46.4	8.35	2.9	1.39
A1	75.4	4.66	2.15	1.04
A1	88.4	1.7	1.3	2.74
A1	102.2	1.3	1.14	2.05
A1	152.5	2.51	2.11	1.58
A1	164	3.0	2.16	1.73
A1	172.5	7.12	2.67	4.09
A1	194.4	3.74	1.94	2.3
A1	223.8	2.5	1.58	1.13
A1	261.5	6.48	2.54	2.54
Symmetry	**f (cm^{-1})**	**I_{633}/I_{514}**	**$\lvert h_{633}\rvert/\lvert h_{514}\rvert$**	
A2	125	2.5	1.58	
A2	184	2.8	1.67	

Table 2. Enhancements factors ($\lvert d_{633}\rvert/\lvert d_{514}\rvert$ and $\lvert f_{633}\rvert/\lvert f_{514}\rvert$) for Raman tensor elements |d|, |f| and |h| as determined from I_{633}/I_{514} for both A_1 and A_2 modes and |d|/|f| values for A_1 modes taken from angular resolved polarized Raman measurements at 633 nm and 514 nm listed in Table 1.

Discussion

In the experiments described above, we have explored Raman scattering from 13 A_1 modes and 6 A_2 modes which are excited using both green (514 nm) and red (633 nm) laser excitation. We have shown that we can extract |d|/|f| and ϕ_{df} for every A_1 mode by fitting the *shape* of the angular dependence of the Raman spectra for $(e_i||e_s)$ using Eq. (3). It is straightforward to show that by combining this data with the intensity ratios, I_{633}/I_{514}, one can extract directly the excitation energy dependence of |d| and |f| directly (S7). Specifically, for A_1 modes which exhibit a maximum intensity for $\theta = 0°$, we find:

$$\frac{|f_{633}|}{|f_{514}|} = \sqrt{\frac{I_{633}}{I_{514}}}\frac{(|d_{514}|/|f_{514}|)}{(|d_{633}|/|f_{633}|)} \tag{8}$$

If the maximum intensity for the mode is at $\theta = 90°$ then:

$$\frac{|f_{633}|}{|f_{514}|} = \sqrt{\frac{I_{633}}{I_{514}}} \tag{9}$$

From this we can extract the ratio for the d Raman tensor element:

$$\frac{|d_{633}|}{|d_{514}|} = \left(\frac{|f_{633}|}{|f_{514}|}\right)\frac{(|d_{633}|/|f_{633}|)}{(|d_{514}|/|f_{514}|)} \tag{10}$$

For the A_2 modes where we can measure the intensity ratios I_{633}/I_{514} which is directly related to the h Raman tensor element:

$$\frac{|h_{633}|}{|h_{514}|} = \sqrt{\frac{I_{633}}{I_{514}}} \tag{11}$$

In Table 2 we show all of the results from these experiments.

While all the A_1 phonon modes essentially have the same symmetries, the modes show a wide range of responses in both intensity and changes in the relative electron–phonon coupling parameters, |d| and |f|. Most modes show a substantial increase in Raman scattering efficiency in the red which range from factors of 2–8 (see Tables 1, 2 or Fig. 6), while two A_1 modes are not seen at all in the green, and two modes do not show any intensity enhancement. Such differing behavior from mode to mode is *not* what is usually seen in resonant Raman experiments. In most cases, all Raman modes are seen to increase in intensity substantially when a virtual intermediate *electronic* state is created and destroyed in the Raman scattering process because the energy denominator in the Raman tensor element tends towards zero for all modes (see denominator of Eq. 1). One concludes that the variation in the intensity and also in |d/|f| must result from differences in the matrix elements in the numerator. An incoming photon creates a real or virtual electronic state which creates a phonon through electron–phonon coupling by scattering to an intermediate electronic state before the electron and hole recombine emitting a photon at a lower energy. To show the wide variation in the energy variation of the Raman tensor elements, we use Eqs. 8–11 to extract $\lvert d_{633}\rvert/\lvert d_{514}\rvert$, $\lvert f_{633}\rvert/\lvert f_{514}\rvert$ and $\lvert h_{633}\rvert/\lvert h_{514}\rvert$. These values are recorded in Table 2. In Fig. 6 we display I_{633}/I_{514}, $\lvert d_{633}\rvert/\lvert d_{514}\rvert$, and $\lvert f_{633}\rvert/\lvert f_{514}\rvert$ as a function of phonon energy for the A_1 phonon modes. One can clearly see strong increases in the Raman scattering efficiencies for red (633 nm) excitation in many of the Raman modes. However, the behavior of |d| and |f| are different. For example, maximum intensity enhancements are seen

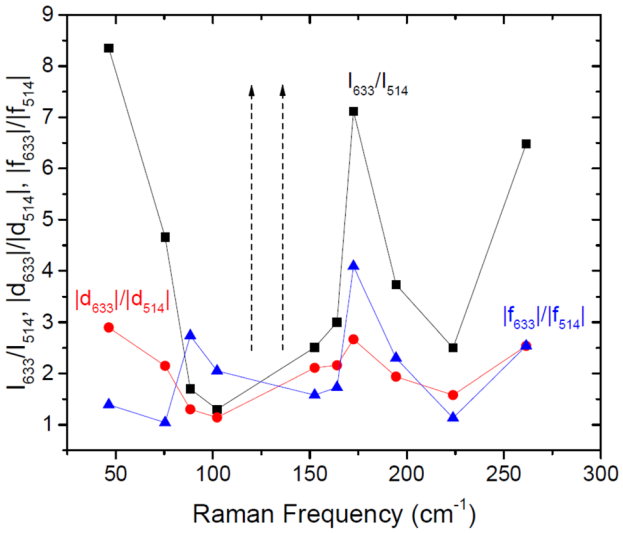

Figure 6. Plot of I_{633}/I_{514} (black sqares), $|d_{633}|/|d_{514}|$ (red circles), and $|f_{633}|/|f_{514}|$ (blue triangles) as a function of phonon energy for A_1 modes. Vertical arrows show modes which are only seen for 633 nm excitation.

for the phonon frequencies at 46.4, 172.4 and 261.2 cm^{-1}. The 46.4 cm^{-1} mode shows that the enhancement for the |d| tensor element is larger than for |f|. However, the 172.4 cm^{-1} mode shows that the enhancement for the |f| tensor element is larger than for |d|, while the 261.2 cm^{-1} phonon shows the same enhancement for |d| and for |f|. More interestingly, there is a peak enhancement in the |f| tensor element where the intensity enhancement is a minimum. It is the variation of the electron–phonon coupling which results in the creation and scattering of phonons which results in such a wide variation in intensities and angular polarization response moving from green to red excitation. A number of theoretical works have shown that the coupling of phonons to the chiral Fermions in these topological Weyl semimetals is quite complex[29,30,32,33] Substantial changes (even Fano resonances) have been observed as a function of temperature for both Raman scattering and also infrared absorption, and also most recently in a magnetic field[34–38,40]. The results here shows that substantial changes can also occur in the electron–phonon coupling during the creation of virtual intermediate states in resonant Raman scattering.

Conclusion

A total of 19 Raman active modes, 13 A_1 and 6 A_2 from $NbIrTe_4$ have been detected through angle-resolved polarized micro-Raman scattering for 633 nm and 514 nm excitations. The frequency and symmetry of the detected modes is consistent with expectations from DFT calculations. The DFT calculations also provide the normal modes for each mode in which A_1 modes have out-of-plane motions while A_2 modes have in-plane motions. Utilizing the symmetry of the A_1 modes, we are able to explore the relative change of the scattering efficiency and |d|/|f| electron–phonon constants as a function of excitation energy for each phonon mode. We observe efficiency increases for the majority of modes for red excitation rather than green, but these increases vary substantially from mode to mode. For example, some modes are unexpectedly absent for green excitation while others are seen to be unchanged for both red and green excitation. Thus, some modes clearly show increases or decreases of the |d|/|f| electron–phonon coupling parameters, while others do not change. Through analysis of these results, we are able to extract the quantitative enhancements of the electron–phonon tensor elements |d|, |f| and |h| for 10 A_1 phonons and 2 A_2 phonons ranging from 5 to 32 meV (45 to 260 cm^{-1}). We conclude that these changes cannot be related to common excitations of the same intermediate electronic states, but rather result from the complex coupling of the phonons with the complex electronic states (possibly the Chiral Fermion states) which have been seen in a number of other systems[34–38].

Methods

NbIrTe4 sample preparation. Single crystals of $NbIrTe_4$ were synthesized via the self-flux method. Nb powder (Alfa, 99.99%), Ir powder (Alfa, 99.95%), and Te shot (99.999%) were sealed in a fused silica ampoule under 10^{-6} Torr of vacuum. The reagents were mixed to yield a solution of 5 at.% $NbIrTe_4$ in Te. The samples were heated to 1000 C at a rate of 200 C/h, soaked at 1000 C for 24 h, and subsequently cooled to 500 C at 2C/h. Molten Te was centrifuged at 500 C to isolate crystals. Crystals present as thin, silver flakes with a metallic luster. Dimensions of 1 mm × 2 mm × 0.1 mm can be achieved under these conditions.

Sample characterization. Lattice parameters of $NbIrTe_4$ were obtained at 300 K using single crystal X-ray diffraction (SCXRD). Data was collected using a Bruker Kappa Apex II single-crystal diffractometer with Mo Ka radiation and a TRIUMPH monochromator.

Angular-dependent Raman scattering measurements. Figure 1d illustrates a schematic diagram of our polarized micro-Raman experiment system. For excitation we have used a polarized 632.8 nm wavelength of a He/Ne laser and a polarized 514.5 nm wavelength of an Argon-ion laser. The laser beam is focused to a ~ 1.5 μm spot size onto the nanoflake by using a 100× objective. The laser power at 633 and 514 nm measurements is limited to less than 200 μW on the sample. The incoming and backscattered laser beams are along the 'c' axis of the flake and the linear polarization of the incident beam is fixed during experiment. By rotating the measurement stage which carries $NbIrTe_4$ flake on a Si/SiO_2 substrate, it is possible to align the incident laser polarization along the 'a' or 'b' axes of the crystal, or any arbitrary angle in between while keeping the laser spot constant on the nanoflake. The backscattered light passes through a polarizer which is fixed to provide the maximum efficiency through a Dilor triple-spectrometer with two 1800 mm^{-1} gratings used in the subtractive mode to remove the scattered laser light followed by a dispersive spectrograph with a 1800 mm^{-1} grating. The signal is detected by a LN2 cooled CCD camera. A half-wave plate before the polarizer is allows us to select the polarization of the scattered light (e_s) to be either parallel ($e_i \parallel e_s$) or perpendicular ($e_i \perp e_s$) to the incident laser polarization (e_i).

DFT calculations of phonon modes. Our calculations are performed using density functional theory (DFT) as implemented in the Vienna ab initio simulation package (VASP) code[50–52]. The Perdew–Burke–Ernzerhof (PBE) exchange–correlation functional and the projector-augmented-wave (PAW) approach are used. Throughout the work, the cutoff energy is set to be 550 eV for expanding the wave functions into plane-wave basis, and the number of k points was set to 4 × 4 × 4 for a 3 × 1 × 1 supercell. The real-space force constants of the supercells were calculated in the density-functional perturbation theory (DFPT)[53] and the phonon frequencies were calculated from the force constants using the PHONOPY code[54]. In our calculations, we adopt the experimental structural parameters (a = 3.7903 Å, b = 12.5207 Å, and c = 13.1435 Å).

Received: 28 December 2020; Accepted: 25 March 2021
Published online: 14 April 2021

References

1. Liu, Z. K. *et al.* Discovery of a three-dimensional topological dirac semimetal, Na_3Bi. *Science (80-)* **343**(6173), 864–867 (2014).
2. Liu, Z. K. *et al.* A stable three-dimensional topological Dirac semimetal Cd_3As_2. *Nat. Mater.* **13**(7), 677–681 (2014).
3. Armitage, N. P., Mele, E. J. & Vishwanath, A. Weyl and Dirac semimetals in three-dimensional solids. *Rev. Mod. Phys.* **90**(1), 015001 (2018).
4. Schoop, L. M., Dai, X., Cava, R. J. & Ilan, R. Special topic on topological semimetals—New directions. APL Mater. **8** (3), 2020.
5. Gao, H., Venderbos, J. W. F., Kim, Y. & Rappe, A. M. Topological semimetals from first principles. *Annu. Rev. Mater. Res.* **49**(1), 153–183 (2019).
6. Riseborough, P. S. & Magalhaes, S. G. Spin-excitons in heavy-fermion semimetals. *J. Magn. Magn. Mater.* **400**, 3–6 (2016).
7. Yan, B. & Felser, C. Topological materials: Weyl semimetals. *Annu. Rev. Condens. Matter Phys.* **8**(1), 337–354 (2016).
8. Yang, B. J. & Nagaosa, N. Classification of stable three-dimensional Dirac semimetals with nontrivial topology. *Nat. Commun.* **5**, 1–10 (2014).
9. Lv, B. Q. *et al.* Experimental discovery of Weyl semimetal TaAs. *Phys. Rev. X* **5**(3), 1–8 (2015).
10. Chang, G. *et al.* Room-temperature magnetic topological Weyl fermion and nodal line semimetal states in half-metallic Heusler Co_2 TiX (X=Si, Ge, or Sn). *Sci. Rep.* **6**(June), 1–9 (2016).
11. Yu, R., Fang, Z., Dai, X. & Weng, H. Topological nodal line semimetals predicted from first-principles calculations. *Front. Phys.* **12**(3), 1–14 (2017).
12. Ruan, J. *et al.* Symmetry-protected ideal Weyl semimetal in HgTe-class materials. *Nat. Commun.* **7**, 1–6 (2016).
13. Lv, B. Q. *et al.* Observation of Weyl nodes in TaAs. *Nat. Phys.* **11**(9), 724–727 (2015).
14. Shekhar, C. *et al.* Extremely large magnetoresistance and ultrahigh mobility in the topological Weyl semimetal candidate NbP. *Nat. Phys.* **11**(8), 645–649 (2015).
15. Kumar Sudesh, P. & Patnaik, S. Origin of exceptional magneto-resistance in Weyl semimetal $TaSb_2$. *J. Phys. Commun.* **3**(11), 115007 (2019).
16. Xiong, J. *et al.* Evidence for the chiral anomaly in the Dirac semimetal Na_3Bi. *Science (80-)* **350**(6259), 413–416 (2015).
17. Chang, C.-Z. *et al.* Experimental observation of the quantum anomalous hall effect in a magnetic topological insulator. *Science (80-)* **340**(6129), 167–170 (2013).
18. Cooper, L. N. *et al.* Quantized anomalous hall effect in. *Science (80-)* **61**(July), 61–64 (2010).
19. Figarova, S. R. Negative longitudinal magneto-resistance of layered crystals taking into account the spin splitting. *Phys. Status Solidi Basic Res.* **243**(6), 41–43 (2006).
20. Ma, J. *et al.* Nonlinear photoresponse of type-II Weyl semimetals. *Nat. Mater.* **18**(5), 476–481 (2019).
21. Wang, H. & Qian, X. Ferroelectric nonlinear anomalous Hall effect in few-layer WTe_2. *npj Comput Mater* **5**(1), 1–8 (2019).
22. Wang, Q. *et al.* Robust edge photocurrent response on layered type II Weyl semimetal WTe_2. *Nat. Commun.* **10**(1), 1–7 (2019).
23. de Juan, F., Grushin, A. G., Morimoto, T. & Moore, J. E. Quantized circular photogalvanic effect in Weyl semimetals. *Nat. Commun.* **8**(May), 15995 (2017).
24. Chan, C.-K., Lee, P. A., Burch, K. S., Han, J. H. & Ran, Y. When chiral photons meet chiral fermions: Photoinduced anomalous hall effects in Weyl semimetals. *Phys. Rev. Lett.* **116**(2), 026805 (2016).
25. McIver, J. W. *et al.* Light-induced anomalous Hall effect in graphene. *Nat. Phys.* **16**(1), 38–41 (2020).
26. Deng, K. *et al.* Experimental observation of topological Fermi arcs in type-II Weyl semimetal MoTe 2. *Nat. Phys.* **12**(12), 1105–1110 (2016).
27. Soluyanov, A. A. *et al.* Type-II Weyl semimetals. *Nature* **527**(7579), 495–498 (2015).
28. Li, P. *et al.* Evidence for topological type-II Weyl semimetal WTe2. *Nat. Commun.* **8**(1), 8–15 (2017).
29. Hui, A., Zhang, Y. & Kim, E. A. Optical signatures of the chiral anomaly in mirror-symmetric Weyl semimetals. *Phys. Rev. B* **100**(8), 1–7 (2019).
30. Rinkel, P., Lopes, P. L. S. & Garate, I. Signatures of the chiral anomaly in phonon dynamics. *Phys. Rev. Lett.* **119**(10), 1–5 (2017).
31. U. Vool *et al.* Imaging phonon-mediated hydrodynamic flow in WTe_2 with cryogenic quantum magnetometry. arXiv:2009.04477 (2020).

32. Song, Z., Zhao, J., Fang, Z. & Dai, X. Detecting the chiral magnetic effect by lattice dynamics in Weyl semimetals. *Phys. Rev. B* **94**(21), 1–7 (2016).
33. Rinkel, P., Lopes, P. L. S. S. & Garate, I. Influence of Landau levels on the phonon dispersion of Weyl semimetals. *Phys. Rev. B* **99**(14), 144301 (2019).
34. Xu, B. *et al.* Temperature-tunable Fano resonance induced by strong coupling between Weyl fermions and phonons in TaAs. *Nat. Commun.* **8**, 8–13 (2017).
35. Osterhoudt, G. B. *et al.* Evidence for dominant phonon-electron scattering in Weyl semimetal WP_2. *Phys. Rev. X* **11**(1), 011017 (2021).
36. Coulter, J. *et al.* Uncovering electron-phonon scattering and phonon dynamics in type-I Weyl semimetals. *Phys. Rev. B* **100**(22), 220301 (2019).
37. Zhang, K. *et al.* Anomalous phonon-mode dependence in polarized Raman spectroscopy of the topological Weyl semimetal TaP. *Phys. Rev. B* **101**(1), 014308 (2020).
38. Yuan, X. *et al.* The discovery of dynamic chiral anomaly in a Weyl semimetal NbAs. *Nat. Commun.* **11**(1), 1–7 (2020).
39. Li, L. *et al.* Ternary Weyl semimetal $NbIrTe^4$ proposed from first-principles calculation. *Phys. Rev. B* **96**(2), 1–7 (2017).
40. Chen, H. *et al.* Unusual polarization and temperature-dependent Raman response in Weyl semimetal $NbIrTe_4$. *Solid State Commun.* **289**(July 2018), 56–60 (2019).
41. Huang, X. W. *et al.* Magneto-transport and Shubnikov-de Haas oscillations in the type-II Weyl semimetal candidate $NbIrTe_4$. *Chinese Phys. Lett.* **36**(7), 092402 (2019).
42. Schönemann, R. *et al.* Bulk fermi surface of the Weyl type-II semimetallic candidate $NbIrTe_4$. *Phys. Rev. B* **99**(19), 195128 (2019).
43. Mar, A. & Ibers, J. A. Synthesis and physical properties of the new layered ternary tellurides $MIrTe_4$ (M = Nb, Ta), and the structure of $NbIrTe_4$. *J. Solid State Chem.* **97**(2), 366–376 (1992).
44. Martin, R. M. & Falicov, L. M. Resonant Raman Scattering. In *Light Scattering in Solids* (ed. Cardona, M.) 79–145 (Springer, 1975).
45. Liu, Y. *et al.* Raman signatures of broken inversion symmetry and in-plane anisotropy in type-II Weyl semimetal candidate $TaIrTe_4$. *Adv. Mater.* **30**(25), 1706402 (2018).
46. Song, Q. *et al.* The in-plane anisotropy of WTe_2 investigated by angle-dependent and polarized Raman spectroscopy. *Sci. Rep.* **6**, 1–9 (2016).
47. Ribeiro, H. B. *et al.* Unusual angular dependence of the Raman response in black phosphorus. *ACS Nano* **9**(4), 4270–4276 (2015).
48. Le Mardelé, F. *et al.* Optical conductivity of the type-II Weyl semimetal $TaIrTe_4$. *Phys. Rev. B* **102**(4), 045201 (2020).
49. Homes, C. C., Ali, M. N. & Cava, R. J. Optical properties of the perfectly compensated semimetal WTe_2. *Phys. Rev. B* **92**(16), 161109 (2015).
50. Kresse, G. & Furthmüller, J. Efficient iterative schemes for ab initio total-energy calculations using a plane-wave basis set. *Phys. Rev. B* **54**(16), 11169–11186 (1996).
51. Kresse, G. & Furthmüller, J. Efficiency of ab-initio total energy calculations for metals and semiconductors using a plane-wave basis set. *Comput. Mater. Sci.* **6**(1), 15–50 (1996).
52. Kresse, G. & Hafner, J. Ab initio molecular dynamics for liquid metals. *Phys. Rev. B* **47**(1), 558–561 (1993).
53. Baroni, S., Giannozzi, P. & Testa, A. Green's-function approach to linear response in solids. *Phys. Rev. Lett.* **58**(18), 1861–1864 (1987).
54. Togo, A., Oba, F. & Tanaka, I. First-principles calculations of the ferroelastic transition between rutile-type and $CaCl_2$-type SiO_2 at high pressures. *Phys. Rev. B* **78**(13), 134106 (2008).

Acknowledgements

We acknowledge the financial support of NSF through grants DMR 1507844, DMR 1531373, DMR 1505549 and ECCS 1509706, and the NSF of China through grant 11674278. S.D.W. and B.R.O. acknowledge support from the University of California Santa Barbara Quantum Foundry, funded by the National Science Foundation (NSF DMR-1906325). Research reported here also made use of shared facilities of the UCSB MRSEC (NSF DMR-1720256). B.R.O. also acknowledges support from the California NanoSystems Institute through the Elings Fellowship program.

Author contributions

I.A.S. assisted by S.P. was primarily responsible for taking the data, analyzing the results and preparation of the figures. B.R.O. and S.D.W. were responsible for preparation of the samples and X.R.D. measurements. C.L. and F.Z. were responsible for the D.F.T. calculations and analysis. G.J., H.E.J. and L.M.S. conceived the experiments, and supervised the analysis. I.A.S., H.E.J. and L.M.S. wrote the manuscript. All authors reviewed the manuscript.

Competing interests

The authors declare no competing interests.

Additional information

Supplementary Information The online version contains supplementary material available at https://doi.org/10.1038/s41598-021-87302-y.

Correspondence and requests for materials should be addressed to L.M.S.

Reprints and permissions information is available at www.nature.com/reprints.

Publisher's note Springer Nature remains neutral with regard to jurisdictional claims in published maps and institutional affiliations.